Reduction and analysis of SUMER data

Luca Teriaca

Klaus Wilhelm

Udo Schühle

Max Planck Institut für Aeronomie
37191 Katlenburg-Lindau, Germany

30 July 2003

Contents

Chapter 1

Instrumentation and data reduction

1.1 The SUMER spectrograph

SUMER is a powerful UV instrument capable of making reliable measurements of bulk motions in the chromosphere, TR and low corona with an accuracy better than 2 km s^{-1} (Wilhelm *et al.* 1997), with a spatial resolution of 1 arcsec (one arcsec at L1 corresponds to 715 km on the Sun) across the slit and 2 arcsec along the slit (Lemaire *et al.* 1997). The basic characteristic, capabilities and operations of SUMER are well described by Wilhelm *et al.* (1995, 1997) and Lemaire *et al.* (1997). The optical design (see Fig. 1.1) is based upon two parabolic mirrors, a plane mirror and a spherical concave grating, all made of silicon carbide (SiC). The first off-axis telescope parabola, which has pointing and scan capabilities, images the Sun on the spectrometer entrance slit. The second off-axis parabola collimates the beam leaving the slit. This beam is then deflected by the plane

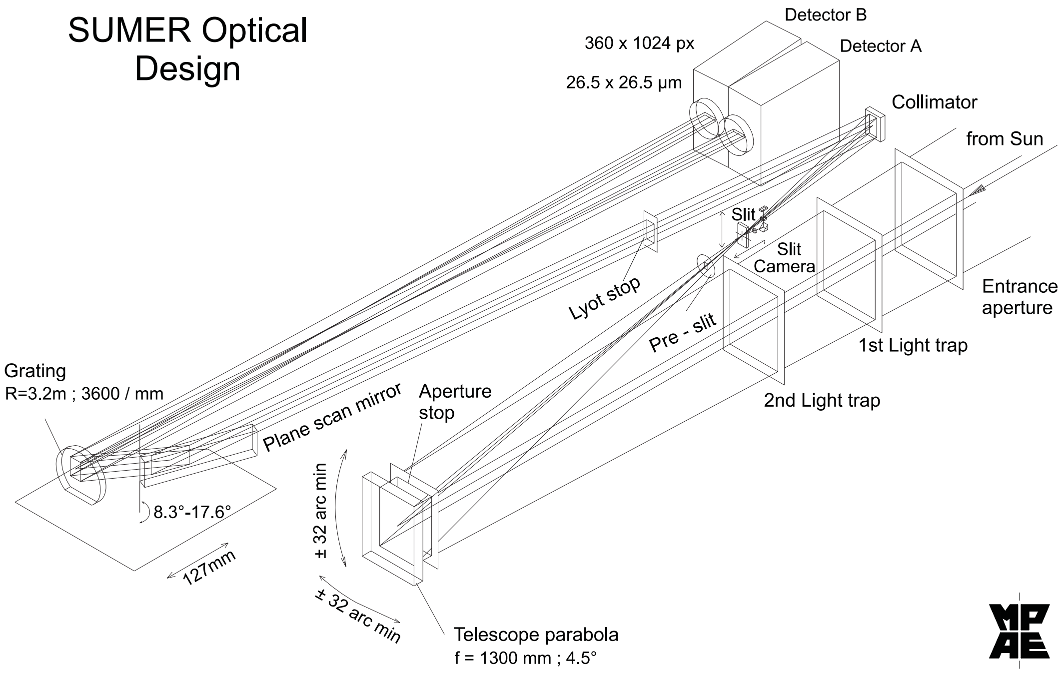

Figure 1.1: Optical layout of the SUMER instrument showing the light-path through the system. The ranges of movements of various mechanisms provided to control the position of the optical components are indicated by arrows. The entrance door and its mechanism are not shown. The spectrometer compartment is completely encapsulated in order to achieve good stray light performance and will only be illuminated through the slit engaged (from Wilhelm *et al.* 1995).

mirror onto the grating. Two detectors (called A and B), located in the focal plane of the concave grating, collect the monochromatic images of the spectrometer entrance slit. The centre of detector A is located on the grating normal, while the centre of the other detector is off by a quantity $\Delta = 70.4$ mm. Coverage of the full spectral range of the instrument requires a wavelength scan performed by rotating the plane mirror. A baffle system, consisting of an entrance aperture, light traps, an aperture stop, a pre-slit and a Lyot stop, completes the design. A brief summary of the basic SUMER optical characteristics is given in Table 1.1 (page 5) The instrument can also provide monochromatic images ("Raster") of selected areas of the Sun by rotating the primary mirror in the east-west direction of elementary steps of 0.3763 arcsec. The scanning capability can also be used to compensate for the solar rotation (Wilhelm *et al.* 1995). Since October 1996, problems with the azimuthal scan mechanism, had prevented the acquisition of raster scans. The raster mode has been once again available from February to November 1999. However, small areas near disk centre could still be scanned using the solar rotation (~ 10 arcsec in one hour at disk centre).

SUMER is equipped with two photon-counting detectors (A and B) with Cross Delay Line readout (XDL) technique (for details see Siegmund *et al.* 1994). However, only one detector can be operated at a time. Each detector has 1024 spectral pixels and 360 spatial pixels. When an exposure is taken, either the full (1024 pixels) spectrum or selected spectral windows (25, 50, 256 or 512 pixels wide) are transmitted to the ground. If the 1×120 or the 0.3×120 arcsec^2 slit is used, it is possible to transmit only the illuminated horizontal band of the detector. The central area of the detectors is coated with a potassium bromide (KBr) layer which increases the detective quantum efficiency up to a factor ~ 20 in the range from 900 Å to 1600 Å (see Fig. 1.2, page 6). In the SUMER spectrograph the diffraction orders are superimposed. The rotation of the flat mirror allows the coverage of the spectral range between 780 and 1610 Å (detector A), thus recording also second order lines between 390 and 805 Å. However, the fall-off of the SiC

Table 1.1: SUMER optical characteristics (extracted from: Wilhelm et al. 1995, with up-to-date values).

Telescope:		
	Focal length	1302.77 mm at 75°C
	Equivalent f-number	10.67
	Plate scale in slit plane	6.316 μm arcsec^{-1}
	Smallest step sizes (N-S and E-W)	0.3763 arcsec
Slits:		
	1	4.122×299.2 arcsec^2
	2	0.986×299.2 arcsec^2
	3	0.993×119.6 arcsec^2 (bottom)
	4	0.993×119.6 arcsec^2 (centered)
	5	0.993×119.6 arcsec^2 (top)
	6	0.278×119.6 arcsec^2 (bottom)
	7	0.278×119.6 arcsec^2 (centered)
	8	0.278×119.6 arcsec^2 (top)
	9	circular hole of 1 arcsec diameter
Spectrometer:		
	Wavelength ranges	
	Detector A	390 – 805 Å (2nd order)*
		780 – 1610 Å (1st order)
	Detector B	330 – 750 Å (2nd order)*
		660 – 1500 Å (1st order)
	Collimator focal length	399.60 mm
	Grating radius	3200.78 mm
	Grating spacing	2777.45 Å (3600.42 lines mm^{-1})
Detectors:		
	Array size	1024 (spectral) $\times$ 360 (spatial) pixels
	Mean spectral pixel size	26.6 μm (Det. A); 26.5 μm (Det. B)
	Mean spatial pixel size	26.5 μm (Det. A); 26.5 μm (Det. B)

* In the range below 500 Å the sensitivity is very low, because of three normal-incidence reflections. Strong lines have, however, been observed in this regime during the calibration phase and under operational conditions.

reflectivity severely reduces the possibility to observe lines at wavelengths below 500 Å. Second order lines (400 – 800 Å) are largely insensitive to the KBr coating (see Fig. 1.4, page 13), allowing us to recognize the second order lines from the first order ones using the different wavelength-dependent sensitivity of KBr compared to the bare part. For this reason, when the entire wavelength range is scanned, every spectrum is partially overlapping the previous and the following,

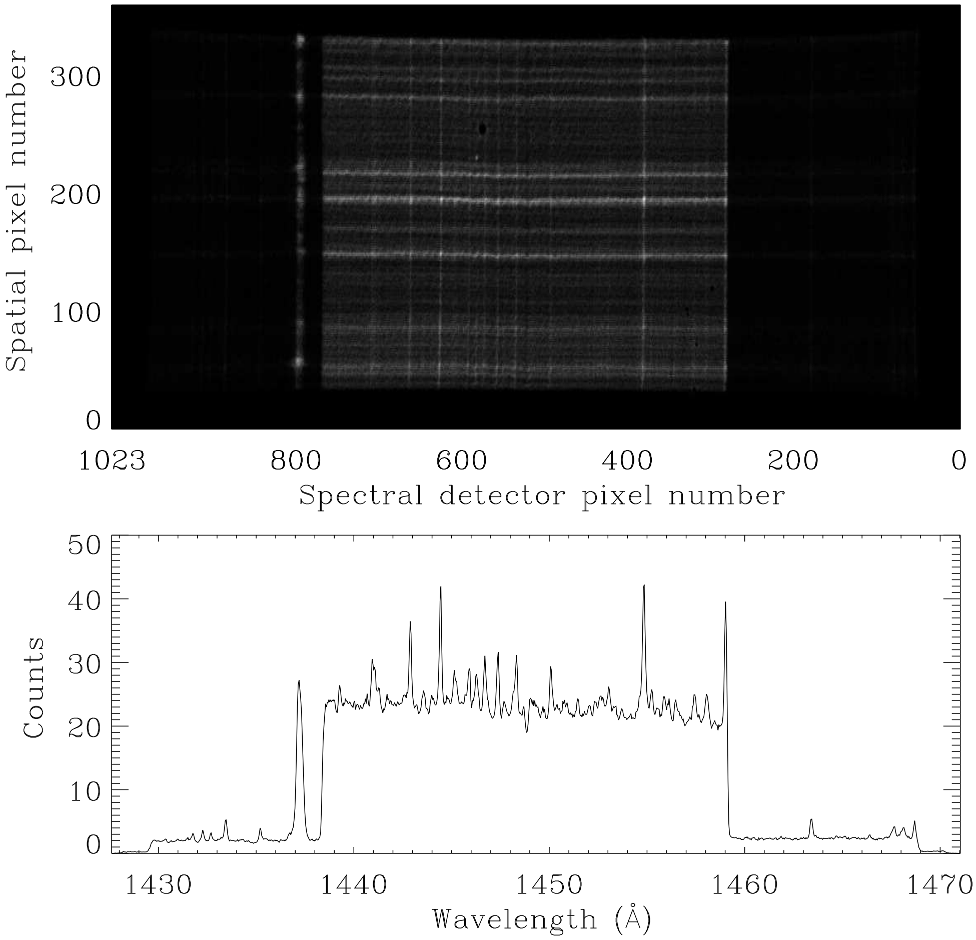

Figure 1.2: SUMER raw UV quiet Sun spectrum around 1450 Å obtained on January 30 1996 at disk centre. The top panel shows the full area of detector A (1024×360 pixel^2) imaged through the 1×300 arcsec^2 slit. In this case only $\sim$ 300 spatial pixels are illuminated. No correction has been applied to the spectrum. The different sensitivity of the KBr coating on the central part of the detector (from detector pixel 280 to 770 in the case of detector A) with respect to the bare part appears immediately evident. At this wavelength the difference in sensitivity is a factor of 10. The geometrical distortion of the image is also evident. The largest detector MCP defect can easily be seen around the pixel coordinates (575, 255). In the lower panel is shown the spectrum obtained averaging along the slit.

in order to ensure that the spectral lines are recorded on both the bare and the KBr parts of the detector.

1.2 SUMER data reduction

SUMER data from the original telemetry are available in two different forms: FITS and IDL-restore files, both produced from GSFC-generated CD-ROMs. The quality will ultimately be the same, but differences exist in the structure of files and the header information. The IDL-restore files contain all of the instrument housekeeping and science data. The FITS data are stored in the SOHO archive at GSFC and the remote sites of the archive, while the IDL-restore files can be produced at MPAe (in Germany) where all SUMER-related CD-ROM data are stored on disk as binary files which are accessible by a Quicklook programme. This allows a quick inspection of a data set before converting the data into restore files. Since May 2001, the MPAe computer centre has set up a web-based system [1] which allows to browse through and, after a password has been granted, download SUMER images as IDL-restore files.

Reduction of SUMER raw images follows several stages, *i.e.* decompression and reversion (for IDL-restore files), dead-time correction, local gain correction, flat-field correction, a correction for geometrical distortion and radiometric calibration (in order to pass from count px^{-1} s^{-1} to Watt m^{-2} sr^{-1} Å^{-1} and to correct for the differences in sensitivity between the KBr and the bare microchannel plate). Some other corrections can also be important in particular cases.

1.2.1 Dead-time & local gain correction

For a total counting rate greater than 5×10^4 event s^{-1}, a correction for the electronic dead-time effect needs to be applied (Wilhelm *et al.* 1995; Hollandt *et al.* 1996). It is important to bear in mind that, whether or not only a part of the detector (sub-format image) is telemetered to the ground, the full detector area has been exposed. Thus, the total count rate on the detector cannot be inferred

[1] http://www.linmpi.mpg.de/english/projekte/sumer/FILE/SumerEntryPage.html

from the total counts in an image if sub-format images are used. In the last case the `XEVENT` and `YEVENT` parameters, that can be obtained from the header of the IDL-restore files (not the FITS or FTS header), needs to be used. Alternatively, if the full spectral image is also available (such an exposure is generally taken in the course of a sequence), it is possible to evaluate the ratio between the counts in the area corresponding to the sub-format image and the counts in the full detector frame. In this case the full detector count rate for each sub-format image can be estimated dividing the total counts in the sub-format image for the above ratio.

Another important effect arises when, for certain bright lines (*i.e.* C III 977 Å or O VI 1032 Å), levels around 10 counts pix^{-1} s^{-1} or higher are reached. In these cases a local reduction in the micro-channel plate (MCP) gain and, therefore, a loss of dynamic range will be present for such strong lines (Wilhelm *et al.* 1997). In addition, long exposures of such bright lines at the same pixel position on the detector will lead to a local reduction in the gain after a certain amount of total counts (total charge) has been extracted. An example of the last effect occurred after the full Sun scan in C III 977 on January 28 1996 which left an imprint of reduced gain around detector (A) pixel 848 (see Fig. 1.2, page 6). In these cases also a correction for the local gain depression needs to be applied at the initial stage. Local gain correction requires dead-time correction to be applied first.

1.2.2 Flat-field correction

Flat-field correction is necessary in order to correct for non-uniformities in the sensitivity of the detector on scales of about 20 pixels or less. Flat-field images are taken approximatively every month with a $\sim$ 3 hour exposure in the Lyman continuum between 860 and 900 Å while the spectrometer grating is defocused (Schühle *et al.* 2000). These are mostly due to a non-linearity of the A/D-converters and the hexagonal pattern of microfiber bundles of the MCPs. In some cases the flat-field correction is performed on board using the last acquired image. The flat-field correction also eliminates or, at least greatly reduces, a modulation of approximatively 19 % every two pixels in the spatial dimension caused by an analogue-to-digital converter differential non-linearity (Siegmund *et al.* 1994). This gives us the possibility to verify whether an image was flat-field corrected or not, simply by comparing a power spectrum of the averaged image along the slit before and after the flat-field correction (Teriaca *et al.* 1999). The disappearance of the peak at period 2 is a clear signature that the flat-field correction has been applied. However, in order to apply this technique, it is important that the spectrum in question is characterized by a sufficiently high signal-to-noise ratio. In Fig. 1.3 (page 10) the Fourier analysis for the quiet Sun spectrum shown in Fig. 1.2 (page 6), before and after the correction with a flat-field taken on 2 February 1996, is presented.

Carlsson, Judge and Wilhelm (1997) found a drift in the fixed pattern of the detector with time, which is caused by scrubbing by the electrons extracted in the channel plates (Griffiths et al. 1998). It is thus a function of the total charge extracted from the channel plates. Since this depends on the location where bright spectral lines have been registered on the active detector area, this is not uniform in time and spatial location. It leads to a non-uniform drift of the fixed pattern, except the 19% pixel-to-pixel variation which is induced by the digitisation. It is thus completely independent of the channel plate usage and is not moved by this effect (Schühle, private communication). This drift can only roughly be interpolated between subsequent flat-field exposures. In this way only a temporal and spatial average of the drift can be determined. Since the 19 % pixel-to-pixel variation, induced by the ADC, is a pattern that is not shifted, it has to be corrected separatly, before a shifted flat-field correction is applied. For this purpose, the SUMER calibration data base provides an image (for A and B detector each) that can be applied to the data by using the flat-field correction routine. This will remove the odd-even row pattern from the data by multiplication of an `ODD_EVEN_ARRAY`. Of course, in this case, flat-fields with the

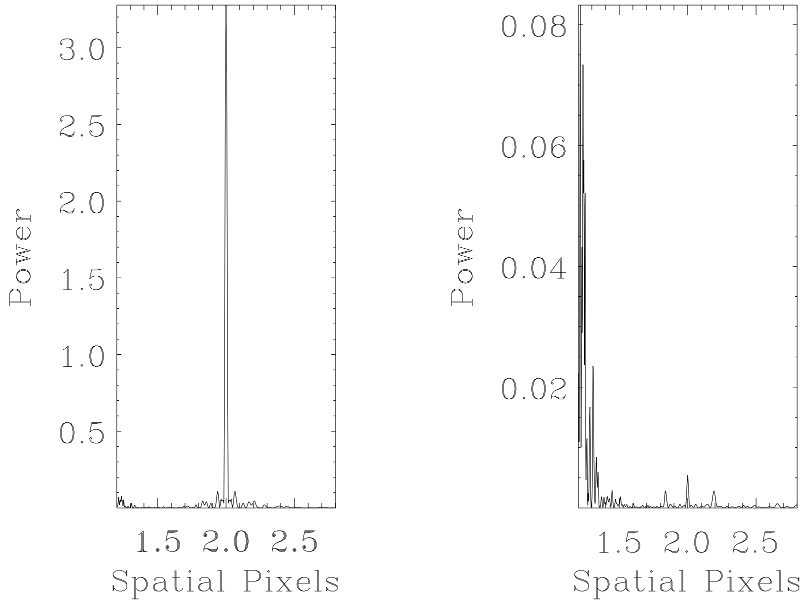

Figure 1.3: Power spectrum of the average along the slit of the Quiet Sun detector image showed in Fig. 1.2 (page 6), before (left panel) and after (right panel) the flat-field correction, showing the reduction in the electronic modulation (see Teriaca *et al.* 1999, for another example).

odd-even pattern removed must be used.

In general, when the data and the closest flat-field are only few days apart, the drift should be small. Teriaca et al. (1999) found a drift of 0.037 pixels (in the spectral direction) between data and a flat-field $\sim$ 3 days apart. This corresponds to approx. 0.4 km s^{-1} at 1250 Å. Such a drift is, however, much smaller then the residual errors in the geometrical distortion correction (see below) and can be ignored. However, attention must be paied when the data and the closest available flat-field are many days apart.

In the case of some particular observations (*e.g.* large rasters of the quiet Sun) a technique to extract the flat-field matrix directly from the data has been described by Dammasch *et al.* (1999).

1.2.3 Geometrical distortion

The analog part of the detector (mainly due to fringe electric fields in the gap between the channel plates and the anode) induce a geometrical distortion of the images of an “inverse cushion” type that is most evident at the extremities of the image. Data for the correction of this distortion have been obtained by producing an artificial grid of horizontal and vertical lines by observing the narrow O I line with Slit 2 (vertical lines) and the Lyman Continuum with Slit 9 (horizontal lines) at many pixel locations of the detectors. The grid data have been used by T. Moran to build correction matrices for each detector (Moran 2002). Different routines all based on `DESTR_BILIN.PRO`, use these matrices as look-up tables to correct the distortion in individual images. However, residual errors remain close to the extremes of the slit (see Fig. 1.5, page 14). Peter (1999a), Peter & Judge (1999) and Judge *et al.* (1998) stress that the geometrical correction routine leaves a residual wavelength error that has a maximum value of ~ 0.2 pixel. As described in the previous paragraph (flat-field correction), the image has shifted with time as the detector has been used (extracted charge). The geometric distortion correction cannot account for this shift: which leaves a residual error in the geometric image correction. It can be adopted an error of 0.15 pixel taking into account these residual effects. This corresponds to an error of ~ 1.5 km s^{-1} around 1250 Å.

1.2.4 Radiometric calibration

The radiometric calibration of the SUMER spectrograph was performed in the laboratory using a secondary source standard, traceable to the Berlin Electron Storage ring for SYnchrotron radiation BESSY I (Hollandt *et al.* 1996). During previous UV space missions, serious losses in sensitivity were observed during the operational life (OSO-6: Huber *et al.* 1973; ATM Reeves *et al.* 1977; OSO-8: Lemaire *et al.* 1991). The degradation is due to the outgassing of organic substances from materials employed in the construction and their subsequent deposition on irradiated surfaces (Steward et al. 1989). In order to reduce possible sources of contamination, a very strict cleanliness program was carried out through all the phases of development of the mission. The stabilities of both detectors has been monitored since the beginning of the operational phase. Results of the first 15 months demonstrate that there was no in-flight degradation experienced (Schühle *et al.* 1998). This monitoring has continued until the present time and no degradation was detected before the loss of attitude of SoHO in June 1998. Thereafter, a loss of responsivity of 43 % (on average) has occurred (Wilhelm *et al.* 2000; Schühle et al. 2003).

In-flight calibration curves were obtained through an iterative process leading to a continual improvement in the final result. Calibration curves were first refined in flight for both orders and for both photocathodes with the help of star data and line ratio methods (Wilhelm *et al.* 1997; Schühle *et al.* 2000). These results have been compared with data from other UV instruments, and particularly from SOLSTICE (Woods *et al.* 1998). After the comparison (Wilhelm et al. 1999), responsivity curves were revised and are now available for the KBr photocathode and the bare MCP, respectively (see Fig. 1.4, page 13). Uncertainties for detector A are estimated to be 15 % from 540 to 1205 Å, 30 % above 1250 Å on KBr. Below 540 Å only very few lines can be observed, and the data need further confirmation. At this stage the uncertainty is estimated to 50 % (1 σ) (Wilhelm *et al.* 2000). The KBr data for detector A in this range need further study. In order to increase the life-time of detector B, in September 1996 it was decided to operate it at a lower gain than during the calibration phase in laboratory. This led to larger uncertainties in the responsivity curves. Uncertainty below 540 Å remains as high as 50 %. In the main part of the spectral range, from 540 Å to 1236 Å, the uncertainty is below 20 % (Schühle *et al.* 2000). The radiometric calibration is performed through the provided software (`RADIOMETRY.PRO`, written by K. Wilhelm). Responsivity curves are subjected to continuous study and can

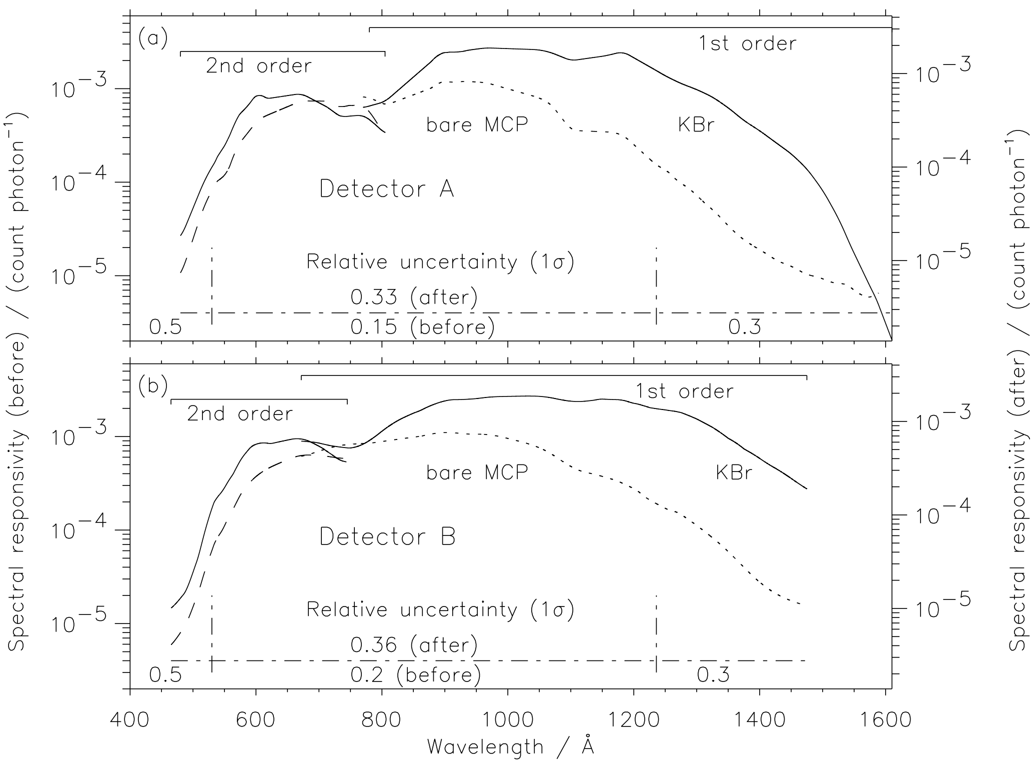

Figure 1.4: Spectral responsivity curves for SUMER detectors A and B, together with the corresponding relative uncertainties for the 1×300 arcsec^2 slit. Above 1250 Å the relative uncertainty relates only to the KBr part of the detectors. The uncertainties shown in the above diagram include the contribution of optical stops and diffraction effects, but the pixel size uncertainty has to be treated separately. In the central wavelength range, detector B shows larger uncertainties due to the lower gain at which the system is operated . Be aware that responsivity curves are updated from time to time and the latest curves should always be used.

be changed from time to time. Hence, it is very important to make sure that the latest calibration is used.

1.2.5 Wavelength calibration

Particular attention needs to be paid to the problem of the wavelength calibration. In the case of SUMER, there is no calibration source aboard, so the wavelength calibration is done using some chromospheric lines of neutral atoms. These lines are formed in the chromosphere at temperatures around 6500 K (*e.g.* Si I and S I, Chae *et al.* 1998a) and are supposed to be at rest (Samain 1991). These lines

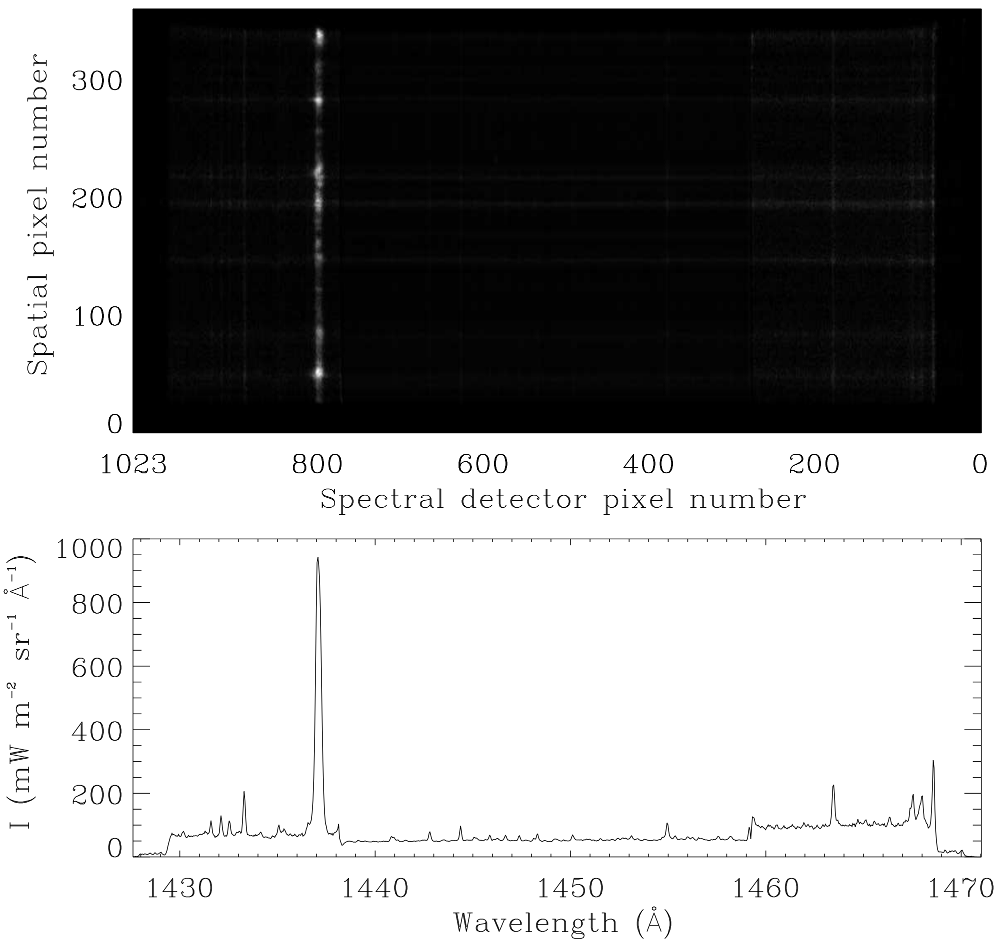

Figure 1.5: SUMER corrected and calibrated UV quiet Sun spectrum around 1450 Å obtained on January 30 1996 at disk centre. The top panel shows the full area of detector A (1024×360 pixel^2) imaged through the 1×300 arcsec^2 slit. In this case only ∼ 300 spatial pixels are illuminated. Dead-time and local gain corrections, flat-field, radiometric calibration and correction for geometrical distortion has been applied to the spectrum (compare with the raw spectrum in Fig. 1.2, page 6). In the lower panel is shown the spectrum obtained averaging along the slit.

should therefore allow the determination of an absolute wavelength scale. Lines such as C I, O I and Fe II are formed at temperatures higher than S I and Si I, (Chae *et al.* 1998a) and can present a certain amount of Doppler shift. Chae *et al.* (1998a) found redshifts of 1.5, 1.8 and 1.8 km s^{-1} for C I, O I and Fe II, respectively. Hassler *et al.* (1991), using the LASP EUV Coronal spectrometer on a sounding rocket flight, found a redshift of 2.7 km s^{-1} for Fe II 1563.790 Å.

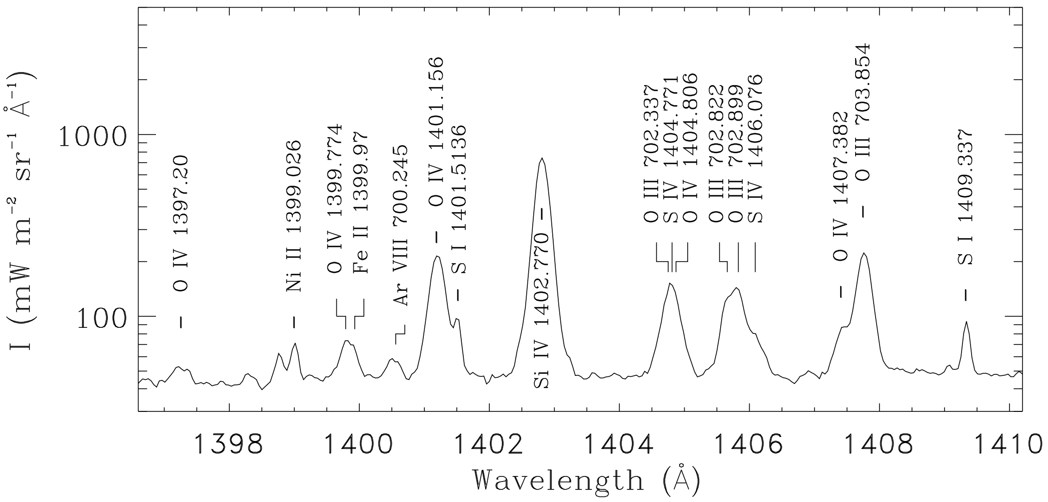

Figure 1.6: SUMER spectrum of the quiet Sun around 1400 Å. The spectrum has been obtained averaging along the slit a full detector exposure obtained on July 10 1996. Note the lines from both first and second order present in this spectral range and, particularly, the ones belonging to the O IV 1400 Å multiplet and, superposed, a group of second order O III lines.

Thus, this amount of Doppler shift should be taken into account before using these lines as zero-point reference. It is important to remember that all the absolute velocity measurements made with SUMER will be relative to those chromospheric reference lines. This also means that, whenever absolute velocity measurements are required, the full spectral detector range (or, at least, half of it) needs to be available in order to have enough reference lines to obtain a reliable wavelength scale. In several cases this is not possible and only velocities relative to average values will be obtained. Chromospheric lines disappear below 900 Å, reducing the wavelength range in which it is possible to make an absolute measure of velocity, to 900 – 1600 Å. However, due to the superposition of the orders, some strong second order lines are recorded against the first order chromospheric lines, thus allowing the precise measure of the central wavelength of important lines such as, e. g., Ne VIII 770.428 (Dammasch *et al.* 1999). In Fig. 1.6 we have an example of a quiet Sun SUMER spectrum recorded around 1400 Å. It is possible to see some second order lines overlapping the first order ones as well as chromospheric lines that can be used for wavelength calibration.

A careful measurement of the absolute line position of several spectral lines across the SUMER spectrum was carried out by Teriaca *et al.* (1999) for two datasets relative to the quiet Sun and to the active region NOAA 7946. In this case almost the entire spectral range between 800 and 1600 Å was covered in several full spectra recorded with detector A.

A preliminary wavelength scale was found for every spectrum using the information contained in the data header (wavelength of reference pixel). In fact, considering the grating equation, we have:

$$m\lambda = d\left(\sin\theta + \sin\alpha\right), \tag{1.1}$$

where m is the diffraction order, d is the grating spacing, θ the angle of incidence on the grating and α the angle of reflection off the grating. In the case of detector A, $\sin\alpha = 0$ while for detector B we have:

$$\sin\alpha_B \approx \frac{\Delta}{f_\lambda}, \tag{1.2}$$

where Δ is the distance between the centres of the two detectors. For a spherical concave grating of radius r_a (= 3200.78 mm), the effective focal length is given by:

$$f_\lambda = \frac{r_a}{1+\cos\theta}. \tag{1.3}$$

Consider the case of detector A ($\cos\alpha = 1$). Differentiating Eq. 1.1 with θ kept constant and assuming $f_\lambda\ d\alpha = dx$ (where dx is the scale of the resolution, given by the pixel size in the spectral direction), we obtain:

$$d\lambda = \frac{d\ Px_A}{m\ f_\lambda}, \tag{1.4}$$

where Px_A is the spectral size of the pixels in detector A (26.6 μm, see Table 1.1, page 5). The dispersion value in the header of FITS files results from the above

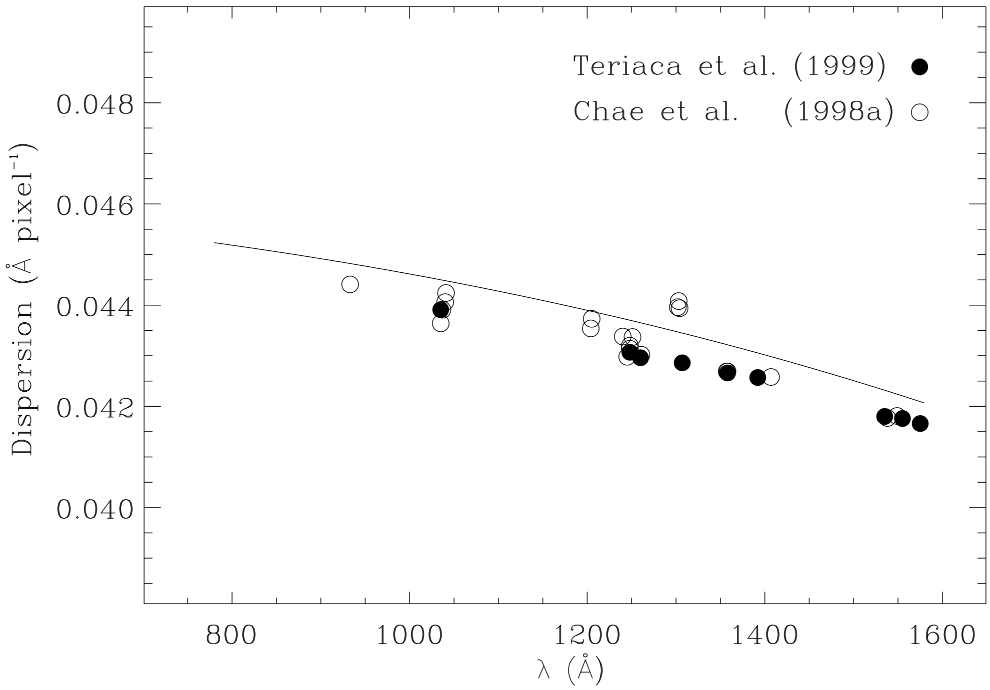

Figure 1.7: Spectral dispersion for detector A: theoretical and observational results. The solid line represents the theoretical dispersion values for Detector A as obtained through Eq. 1.5 (page 17). Dispersion values obtained using chromospheric lines are also shown. Results represented by filled circles are from Teriaca *et al.* (1999), while open circles indicate values obtained by Chae *et al.* (1998a).

equation. Combining Eqs. 1.1, 1.3 and 1.4, we can write the dispersion as a function of the wavelength for detector A,

$$d\lambda = \left[\frac{d \; Px_A \left[1 + \left[1 - \left(\frac{m\lambda}{d} \right)^2 \right]^{1/2} \right]}{m \; r_a} \right] . \tag{1.5}$$

The above equation can be used to build-up a preliminary dispersion relation, which is used as a starting point for the identification of the chromospheric spectral lines present in the spectra. Lists of lines observed on the Sun (on disk and off disk) are available in the literature (Curdt *et al.* 1997a, 2001; Kink *et al.* 1997; Feldman *et al.* 1997; Sandlin *et al.* 1986; Noyes *et al.* 1985; Cohen *et al.* 1978; Vernazza & Reeves 1978; Behring *et al.* 1976). For laboratory wavelengths of UV spectral lines, a large dataset can be found in the literature (Kelly 1982, 1985, 1987) and on the Internet (Harvard-Smithsonian Center for Astrophysics Databases[2]; National Institute of Standard and Technology on-line energy level database).

After having identified as many chromospheric lines as possible, a Gaussian fit was applied to each one in order to derive its central position (in pixels). For each region of interest the dispersion relation was, hence, calculated performing a first order polynomial fit to the pairs 'central pixel'-'laboratory wavelength' of the reference lines. This allows us to determine an absolute wavelength scale, making it possible to measure the central wavelength of all the other spectral lines. The use of a first order fit implies the assumption that the dispersion relation is locally linear. This assumption can be defended observing that the theoretical dispersion obtained from Eq. 1.5 (see also Fig. 1.7) shows a small dependence on the wavelength, so that it can be considered constant in intervals of ~ 20 Å. The derived dispersion values are reported in Table 1.2 (page 19). In Fig. 1.7 the dispersion values reported in Table 1.2 are shown together with the results obtained by Chae *et al.* (1998a) and with the theoretical trend from Eq. 1.5. It can be noted how both the results from Teriaca *et al.* (1999) and Chae *et al.* (1998a) are slightly lower than the values obtained through Eq. 1.5. Generally the laboratory wavelengths of chromospheric lines are well known, with errors much smaller than 1 km s^{-1}.

1.2.6 Additional corrections

After having applied all the above corrections, the spectra are ready to be analyzed. However, there are some other corrections that are important to apply in particular cases.

[2] http://cfa-www.harvard.edu/amdata/ampdata/amdata.html

Table 1.2: Dispersion values for different spectral regions as measured in the Quiet Sun and in Active Region NOAA 7946. Wavelengths for Iron lines are taken from Kelly (1985), all the others from Kelly (1982). In the first column, together with the spectral range, are also listed some of the ionic lines present in that range.

Spectral Range Å	Ref. line	Disp. (Å/pix)
1560 - 1590 (AR)	Fe II 1563.790	0.04166
	Fe II 1569.674	
S V	Fe II 1570.244	
O IV	Fe II 1571.137	
	Fe II 1581.270	
	Fe II 1584.952	
	Fe II 1588.290	
1540 - 1570 (AR)	Fe II 1550.274	0.04176
	Fe II 1559.085	
C IV	Fe II 1563.790	
	Fe II 1569.674	
	Fe II 1570.244	
1520 - 1550 (QS)	Si II 1526.7076	0.04180
	Si II 1533.4320	
Ne VIII	C I 1542.1766	
1380 - 1405 (AR)	Fe II 1387.219	0.04257
	Fe II 1392.149	
O IV	S I 1392.5878	
Si IV	Fe II 1392.817	
Ar VIII	S I 1401.5136	
1350 - 1365 (AR)	C I 1354.288	0.04266
	C I 1355.844	
Na IX	C I 1357.134	
O I	C I 1357.659	
	C I 1358.188	
	C I 1359.275	
	C I 1359.438	
	C I 1364.164	
1295 - 1320 (AR)	S I 1295.6526	0.04286
	S I 1300.907	
Si II	C I 1310.637	
Si III	C I 1311.363	
	C I 1311.924	
	C I 1312.247	
1250 - 1270 (AR)	C I 1254.513	0.04296
	Si I 1258.795	
O V	S I 1262.8596	
	S I 1270.7821	
1240 - 1255 (AR)	C I 1244.535	0.04307
	C I 1245.943	
N V	C I 1249.004	
Fe XII	C I 1249.405	
	C I 1252.208	
	C I 1254.513	
1025 - 1045 (QS)	O I 1027.4307	0.04391
	O I 1028.1571	
C II	O I 1039.2304	
O VI	O I 1040.9425	
	O I 1041.6876	

1.2.6.1 Instrumental broadening

This is a problem common to any spectroscopic analysis and concerns the fact that recorded line profiles are the result of the convolution of the instrumental profile with the true flux spectrum (Gray 1992). Emission lines arising from optically thin transition region and coronal plasma can be considered Gaussian in shape to a very good approximation (Mariska 1992). This is not strictly true for the instrumental profile. This implies that, in theory, the recorded spectral profiles should be not Gaussian in shape leading to the necessity of deconvolution processes of the data in order to extract the "true" spectrum. This is not a trivial operation with complications coming from the almost unavoidable presence of noise, data sampling and windowing (Gray 1992). Moreover, in order to perform the reconstruction process we should have the instrumental profiles for all the possible detector-grating angle-slit combinations. These profiles can be obtained in laboratory before the launch, but not during the flight (there are no calibration lamps aboard). However, in the large majority of cases (outside dynamic events and for lines formed in an optically thin plasma), SUMER line profiles can be fitted reasonably well by a single Gaussian. This demonstrates that the deformations in the observed line shapes induced by the instrumental profiles are indeed not important. This allows us to greatly simplify the problem by correcting only the measured full width at half maximum (FWHM). Tables of deconvolved values have been obtained for the different slits at different wavelength for both detectors. It is, hence, possible to correct the measured FWHM for the contribution of the instrumental profile using the provided software (`CON_WIDTH_FUNCT_3.PRO`, written by K. Wilhelm, based on P. Lemaire calculations). Chae *et al.* (1998b) applied a Gaussian fitting technique to several Pt lines that were emitted by a hollow cathode source and recorded with detector A before launch, finding a FWHM of 1.95 pixels that do not show any significant dependence on the line wavelength. The same authors have also verified that the instrumental broadening has not

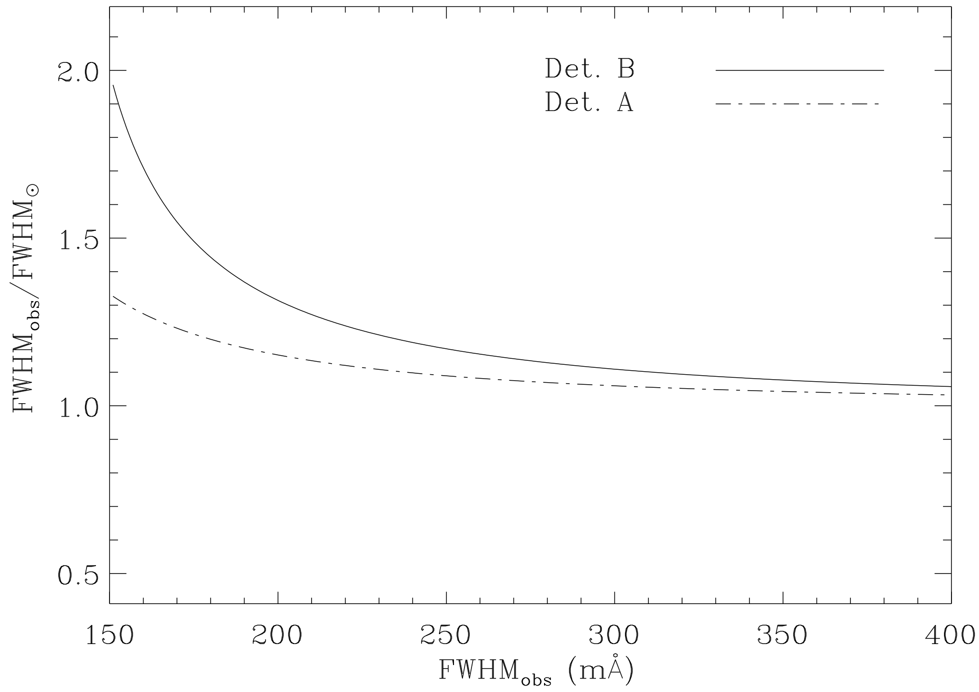

Figure 1.8: The ratio between the observed FWHM (FWHM$_{obs}$) and the corrected one (FWHM$_{\odot}$) is shown for both detectors as a function of FWHM$_{obs}$.

deviated from laboratory values during the operational life of the instrument (at least not until August 1996). In Fig. 1.8 (page 21), the ratio between the observed FWHM (FWHM$_{obs}$) and the corrected one (FWHM$_{\odot}$) is shown for both detectors as a function of FWHM$_{obs}$. It is evident how the importance of the correction decreases for the wider lines (FWHM$_{obs}$ > 300 mÅ).

1.2.6.2 Slit magnification and displacement

The existence of a discrepancy between the orientation of the grating and the detector, causes the spectrum to be inclined with respect to the detector horizontal lines. This leads to a change in the vertical position of the slit image on the detector plane as a function of wavelength. Moreover, the position of the slit image on the detector is also shifted due to the nonlinearity of the grating focus mechanism which is moved simultaneously with the wavelength scan. And, last but not least, there may be a residual angle between the scan mirror rotation axis and the detector vertical lines, which may contribute to the displacement of the slit image.

Besides the displacement of the whole slit image, its projected size on the detector plane is also wavelength dependent. The scale of the Sun image focused by the primary mirror on the slit plane is 6.316 μm arcsec^{-1}. This leads the long (1.89 mm) slit to cover 299.2 arcsec while the short (0.755 mm) slit will cover 119.6 arcsec (see Table 1.1, page 5). The slit is then projected by the collimator over the grating, which will finally focus monochromatic images of the slit onto the detectors (see Fig. 1.1, page 3). The final size of the slit image on the detector plane is determined by the ratio between the grating effective focal length f_λ and the collimator focal length f_c, the so-called *magnification factor*. In the case of detector A ($\sin\alpha = 0$), combining Eqs. 1.1 and 1.3 (page 16) we can easily obtain the magnification factor m_f as a function of wavelength,

$$m_f = \frac{r_a}{f_c \left[1 + \left[1 - \left(\frac{m\lambda}{d}\right)^2\right]^{1/2}\right]}. \tag{1.6}$$

Using the value obtained from Eq. 1.6, we finally obtain the spatial scale of the image on the plane of detector A as:

$$Spatial\ scale\ (Det.\ A) = \frac{Py_A}{6.316\ m_f}, \tag{1.7}$$

where Py_A is the spatial size of the detector pixels (26.5 μm, see Table 1.1 on page 5). From the last equation it is easy to calculate that the long slit will cover 291 and 315 spatial pixels of detector A at 800 Å and 1600 Å respectively. In Fig. 1.9a (page 23), the spatial scale of the slit image on the detector planes are shown as a function of the wavelength for both detectors.

The combined effects of the slit image displacement and magnification trans-

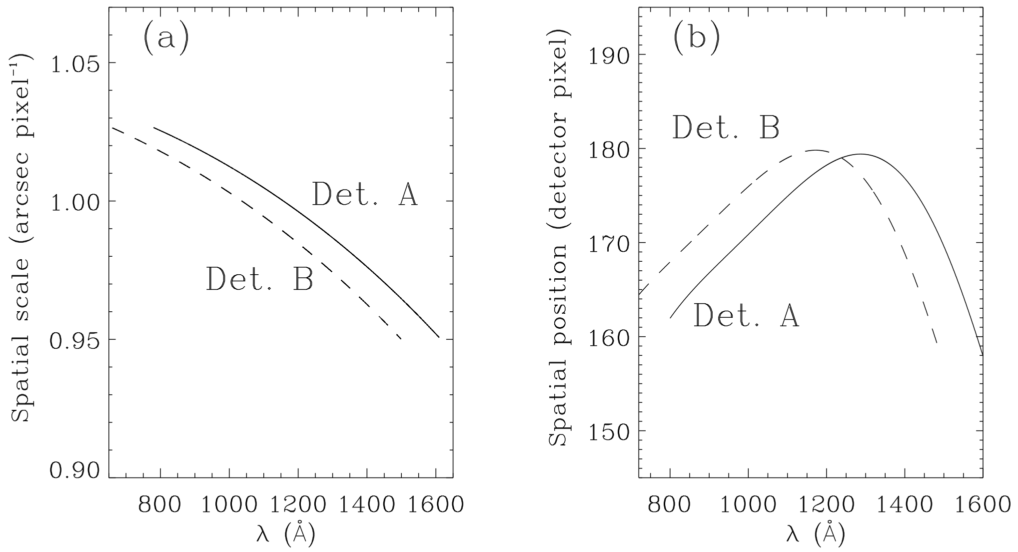

Figure 1.9: Slit image scale and spatial displacement on the detector planes as a function of wavelength. *(a)*: Image spatial scale as function of wavelength on detectors A (solid line) and B (dashed line). *(b)*: Spatial position (in detector pixels) of a point of the slit image, falling on detector pixel 179 at 1238 Å, as a function of wavelength in the cases of detector A (solid line) and B (dashed line).

late into the fact that, as an example, a solar feature recorded on detector A spatial pixel 179 at 1238 Å (N V) will be recorded around pixel 164 when observed at 1548 Å (C IV). The amount of displacement can be as high as 21 spatial pixels, corresponding to $\sim$ 15000 km on the Sun surface. In Fig. 1.9b (page 23) the spatial position (in detector pixels) of a point of the slit image falling on detector pixel 179 at 1238 Å, is shown as a function of wavelength for both detectors. The above correction needs to be applied only when comparing images obtained at different wavelengths. The vertical displacement and spatial scale of the slit image as a function of wavelength can be determined using the provided software (`DELTA_PIXEL.PRO` and `MAGNIFICATION.PRO`, respectively).

1.2.6.3 Long- and short-time instrumental periodicities

Despite the very high thermal and mechanical stability characterizing the instrument (the temperature inside the spectrometer compartment being controlled to within ± 0.15 K, Wilhelm *et al.* 1997), a drift of the whole spectral image has been detected by Curdt *et al.* (1997b). This periodic drift is due to *thermoelastic oscillations*. It was later found also by Dammasch *et al.* (1999), Peter (1999a, 1999b), Muglach & Fleck (1999) and Rybák *et al.* (1999a). In all these cases, the authors report a periodic drift with an amplitude up to 1 pixel and a periodicity of 1-2 hours. We interpreted these oscillations as the effect of mechanical deformations of the spectrometer structure due to small temperature changes induced by the spectrometer heaters. The drift can be avoided by switching off the heaters during the observational sequence (W. Curdt, personal communication). The problem appears whenever a sequence involves a considerable amount of time. This is true in the case of temporal series (*i.e.* sequences of spectra obtained keeping the slit fixed over the same point on the solar surface) devoted to the study of solar chromospheric, transition region and coronal oscillations as well as in raster scans (the slit is moved to an adjacent position after each exposure) of large areas of the solar surface. The drift can assessed looking at the behaviour of the mean line position averaged over all the individual line positions along the slit. In fact, the average along the slit greatly reduces the variations of solar origin, and the large scale variations of the mean position through the dataset will underline the presence of the instrumental drift. A spline fit, or a smoothing procedure, can be applied to the mean line position in order to remove residual variations of solar origin, obtaining a good estimation of the large-scale instrumental drift (see Fig. 2 in Peter 1999a and discussion therein). The drift so obtained can hence be subtracted. Of course, the determination of the drift is more accurate when it can be obtained averaging the results of various lines.

A possible problem also exists for temporal series during which a compensating for the solar rotation is applied (Rybák *et al.* 1999b). These authors suggest that the stepping mechanism could introduce spurious frequencies in the power spectrum of solar oscillations. In the case of temporal series obtained without compensation for the solar rotation there is no problem of introducing short-period variations, but attention has to be paid to the fact that features drift across the strip of solar surface imaged by the slit.

Chapter 2

Observations and data analysis

The SoHO spacecraft and its 12 experiments allow us to observe the Sun from its central core up to the extended corona. In particular, the SUMER spectrograph is able to obtain spectra and monochromatic images of the solar chromosphere, transition region and low corona with high spatial, spectral and temporal resolution. The pointing mechanism of the instrument allows coverage of the entire solar disk and its surroundings up to 1 $R_\odot$ above the limb, permitting observational sequences devoted to the study of different regions of the solar atmosphere. In this Chapter a description of the principal data analysis techniques is presented.

2.1 Observations

As already mentioned, the SUMER spectrograph allows several different types of observational sequences, often complementing one another. In the *spectral scan*, the entire wavelength range is scanned, taking care to record each line with both the KBr and the bare part of the detector (in order to distinguish between first and second order lines). In the *raster scan*, a specific area of the Sun surface (but also of its corona) is scanned moving the slit in the direction perpendicular to the slit itself. Often, essentially because of constraints due to the telemetry rate and to the available memory on board, only selected spectral windows are telemetered to the ground. In the *temporal serial*, the slit is kept on a fixed location and successive spectra are taken at the same central wavelength. In the *spatial spectrum* a single, full detector spectrum, is obtained with high exposure time. This last type of observation is often prior to and after the *raster scan* and the *temporal serial* sequences in order to provide the full reference detector image from which the line(s) used in the temporal or raster sequences are extracted. In *half detector*, a subframe of 512 spectral pixels by 360 spatial pixel is telemetered to the ground.

After recording, the data can undergo a compression procedure, in order to reduce the transmission time (see Wilhelm *et al.* 1995 for more details). Images are, hence, telemetered to the ground together with a descriptional header, containing information about the performed observations (*e.g.* exposure time, central wavelength-reference pixel, slit and detector used, etc). These raw data are stored on CD–ROMs by NASA, and they are also stored as FITS (Flexible Image Transport System) files in the EOF (Experimenters' Operation Facility) at the Goddard Space Flight Center (GSFC) in Washington D.C. These FITS files contain an additional descriptive header, including information from the planning process. Starting from January 1996, the FITS files are currently reprocessed from the original CD–ROM data, with the purpose of improving the quality and removing data faults. The reprocessed data are saved with the extension .FTS (instead of .FITS). It is of fundamental importance to bear in mind that SUMER is fixed "head-down" on SoHO, hence the north direction on the Sun is towards the bottom of the detectors (*i.e.* images are upside-down). This has been changed in the reprocessed (.FTS) files where the north on the Sun is on the top of the image. Data can be found in both formats, and special care need to be paid to the problem when writing the reduction and analysis software.

2.1.1 Solar Rotation Compensation

Compensation of the solar rotation is achieved by moving the slit westward of a given number of elementary steps. If the default rotational compensation is chosen (ROTCOMP=0) then a double step ($\sim$0.76 arcsec) is performed every Δt seconds, where Δt is a function of the pointing coordinates and of the distance between SOHO and the sub-SOHO point (see Wilhelm et al. 1995). The rotational compensation can also be personalized by providing the time interval after wich a double step is performed. Of course, the compensation can also be performed by providing starting coordinates, for each spectroheliogram of a series, that account for the interlapsed rotation.

It is important to underline that the rotation compensation is NOT applied within a raster or a temporal series (defined as a spectroheliogram with spatial increment equal to zero) even if the rotation compensation was enabled during the study. As an example let us consider a study consisting of 2 rasters of a region around Sun centre and that the standard rotation compensation is ON. Let also assume that the observed area is covered in 89 steps of 1.13 arcsec (3 elementary steps) each one followed by a 40 seconds exposure. This mean that each raster lasts one hour and covers formally a 100 arcsec wide region. However, because the rotation compensation is not active during each raster and the solar rotation is around 10 arcsec/hour at disk centre, each raster will cover an area that is 10 arcsec wider or smaller, depending on whether the raster is achieved stepping eastward or westward. This is relevant when comparing a raster with an image (e.g., with a magnetogram).Moreover, because the rotation compensation is active during the study, the second raster will start at a pointing position 10 arcsec westward with respect to the starting position of the first raster. If a finer rotation compensation is required, this can be achieved by using several short rasters instead of a large one.

In the case of temporal series, the rotation compensation can be introduced using several small sequences, each one lasting the time after which the Sun has rotated of 0.76 arcsecs (see § 1.2.6.3, page 23) for possible inconvinients).

2.2 Data Analysis

2.2.1 Binning and averaging along the slit

The search for a compromise between the desire to obtain high (spatial, spectral and temporal) resolution observations and the need of a sufficiently high signal-to-noise to extract the requested information from the data, is a well known problem in astronomical observation in general and in spectroscopic analysis in particular. Thus, in some cases, the original data can be binned (in space and/or in time) in order to achieve a level of signal adequate to the specific analysis performed. The amount of binning, when necessary, needs to be carefully estimated in order to loose the minimum amount of information. Binning should be performed through a simple average of the reduced spectral profiles.

Brynildsen *et al.* (1998) have examined some SUMER and CDS images producing velocity maps (absolute for SUMER data and relative to the average velocity for CDS) in which they show an evident correlation between the observed redshift and the intensity of the line. Compared to the average wavelength position there is a tendency for the wavelength of the lines to change from blueshift to redshift as the peak intensity increases. Using SUMER observations in O VI and C II, Warren *et al.* (1997) found a slight dependence of line position and width on the intensity. Landi *et al.* (2000) divided a SUMER dataset in intensity bins and averaged all the profiles inside each bin, obtaining a high signal-to-noise spectrum for each intensity interval. A plot of the line parameters of these spectra against their intensity shows a clear dependence of both width and Doppler shift. There is, furthermore, evidence of a temporal, sometimes periodic, behaviour of the observed line shifts. This means that the (blue-) redshift phenomenon is of a statistical nature, with strong local variations in the observed Doppler shift in all the transition region lines. This last point is particularly important whenever we are interested in the measurement of the absolute amount of line shift presented by spectral lines. As discussed in § 1.2.5 (page 13) this is done using chromospheric lines to provide the wavelength calibration. However, these lines are usually quite weak and an average over several spatial positions is necessary in order to build-up a spectrum with a high signal-to-noise ratio. Also the short 120 arcsec slit is likely to cross more than one network region when used on the quiet Sun.

If a simple average (along the slit or over a whole image) is made, the locations with high redshift, being on average the most "intense", will dominate and the averaged value will be shifted towards more red shifted values. To avoid this, it is necessary to take some precautions. Chae *et al.* (1998a), solved the problem performing a weighted average along the slit, *i.e.* they normalize the line profile by the integrated intensity before an average is taken. Brynildsen *et al.* (1998), calculated the shift in every position along the slit and, afterwards performed the average along the slit. The last authors showed that the values obtained in this way are systematically lower that the ones obtained with a simple average, especially in active regions. It is also interesting to underline that they found practically no differential velocity between active and quiet regions, but this difference is present when they perform a simple average (with a maximum value around 5 km s^{-1} in O V). Teriaca *et al.* (1999) adopted the idea of Chae *et al.* (1998a) but they have also performed an average on the values calculated for every single spatial pixel for some spectra with very high signal-to-noise ratios. No relevant difference between the two methods was found.

2.2.2 Line identification

The identification of the spectral lines present in a given spectrum is carried out through an extensive research in the literature (several works listing lines observed on- and off-disk are reported on page 16, together with references to works reporting laboratory wavelengths). The identification of ionic lines can be helped by over-plotting the SUMER spectrum with a synthetic one, generated (for both orders) by the CHIANTI database (Dere *et al.* 1997; Landi *et al.* 1999). CHIANTI consists of a critically evaluated set of atomic data necessary to calculate the emission line spectrum of astrophysical plasma. It does not include transitions from neutral atoms. The data consist of atomic energy levels, atomic radiative data such as wavelengths, weighted oscillator strengths and A values, and electron collisional excitation rates. A set of programs that use these data to calculate the

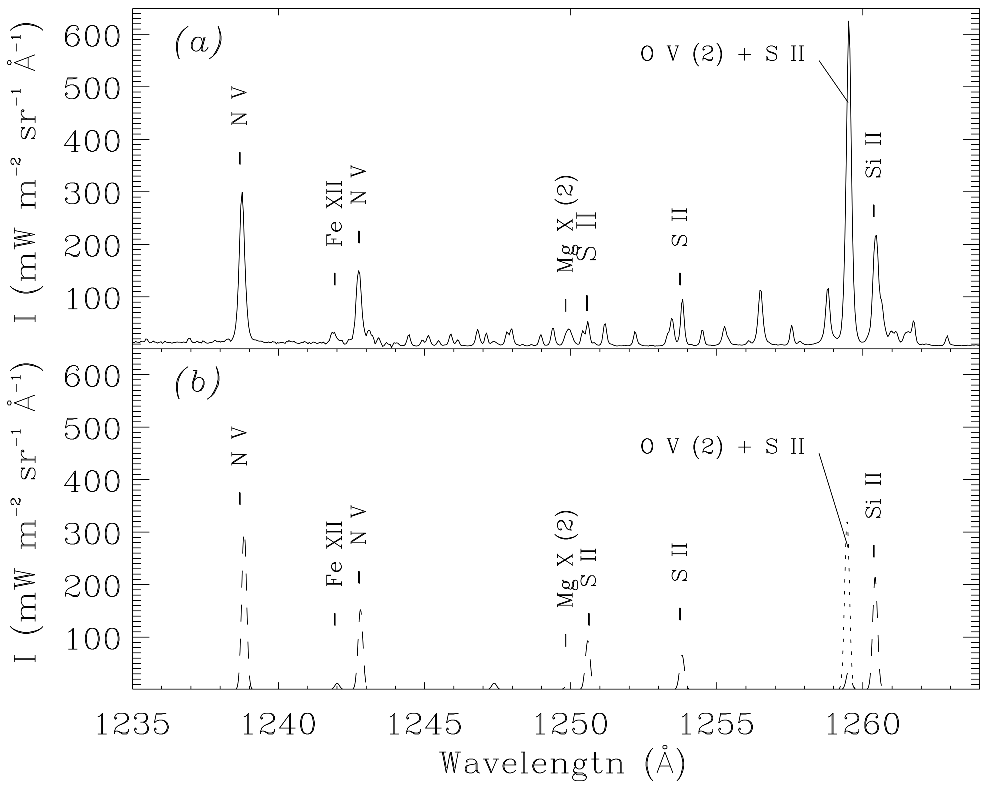

Figure 2.1: Comparison between SUMER quiet Sun spectrum (*top panel*) and CHIANTI synthetic spectrum (*bottom panel*) of first (*dashed line*) and second order (*dotted line).* Note the O V 629 Å and the Mg X 625 Å second order lines.

spectrum in a desired wavelength range as a function of temperature and density are also provided. These programs are written in Interactive Data Language (IDL), making it easy to couple them with the data reduction and analysis software. CHIANTI assumes an optically thin, low density static plasma in ionization and thermal equilibrium. In Fig. 2.1 (page 32) and Fig. 2.2 (page 33) two examples of SUMER spectra are shown (*upper panels*) with superimposed the synthetic spectra (*lower panels*) of first (*dashes line*) and second order (*dotted line*). The CHIANTI spectra were obtained using ionization equilibrium calculations from Mazzotta *et al.* (1998) and abundances values as measured by Grevesse & Sauval (1998) for quiet Sun and by Waljeski *et al.* (1994) for the active region spectrum.

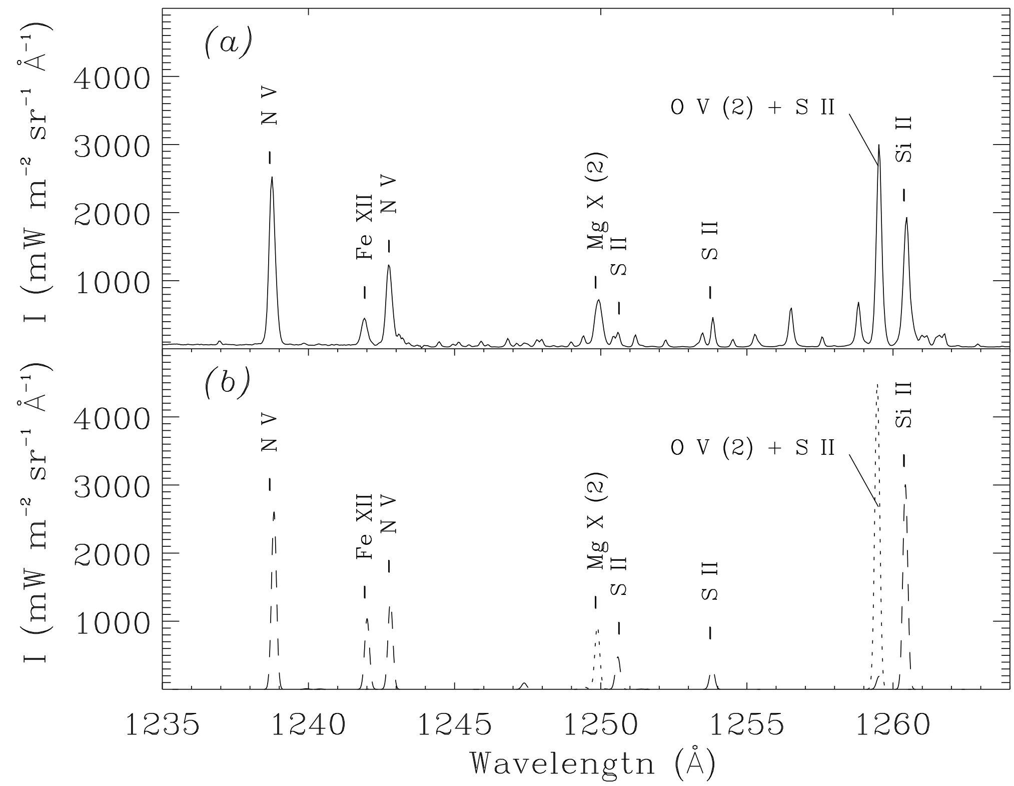

Figure 2.2: Comparison between SUMER active region spectrum (*top panel*) and CHIANTI synthetic spectrum (*bottom panel*) of first (*dashed line*) and second order (*dotted line*). Note the O v 629 Å and the Mg x 625 Å second order lines.

2.2.3 Stray light correction

Despite the very high quality of the telescope mirror, the level of scattered light is not negligible when observations of spectral lines which are bright on disk (*e.g.* O vi, C iii and L_β) are carried out above the limb in faint regions such as Polar Coronal Holes (Lemaire *et al.* 1997; David *et al.* 1998). Here is reported as an example the analysis performed by Banerjee *et al.* (2000) of a dataset obtained in June 1996 in the north polar coronal hole plume and inter-plume regions. An estimation of the stray light contribution to the O vi 1032 Å line profile can be made using a purely chromospheric line such as C ii 1037 Å (Hassler *et al.* 1997). This line does not have any coronal contribution and is, hence, entirely due to stray light. Fig 2.3 (page 34) shows the behaviour of the intensity with height above the limb for O VI 1037 Å and C II 1037 Å lines. Note the contrast between plume and inter-plume in O VI. If C II emission is due only to scattered light we would not expect any difference between plume and inter-plume (Hassler *et al.* 1997). The difference noted in Fig. 2.3 near the disk is due to the difficulty of fitting the C II line particularly when it is only a tiny fraction of the nearby O VI 1037 Å line. Furthermore a proper fit of the C II 1037 Å line was difficult because the spectra nearest to the disk (up to ~ 1.2 $R_\odot$) were only 50 pixel wide. These problems lead essentially to an overestimation of the line width of C II near the limb. In fact, it has been verified that the peak intensity for C II shows the same values in plume and inter-plume. Data relative to inter-plume were, hence, used for the calculation of the stray light contribution. The O VI 1032 stray light intensity at a certain altitude above the limb will be given by the product of the C II 1037 intensity at that altitude times the ratio of the disk-averaged O VI 1032 and C II 1037 line intensities. The above ratio and the stray light profile in O VI 1032 Å were evaluated using observations at 1.8 $R_\odot$, where the SUMER spectrum

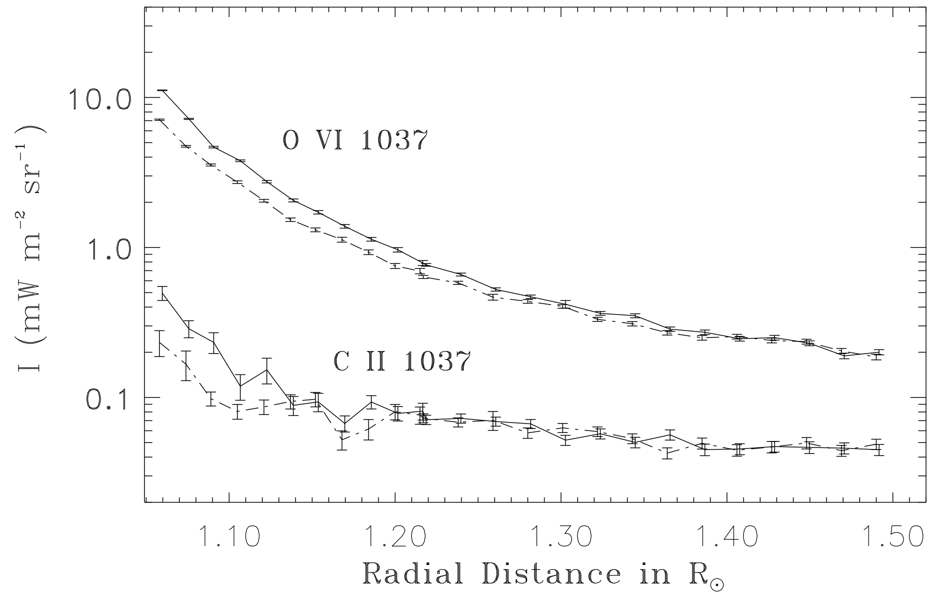

Figure 2.3: Variation of the intensity with height along a polar plume (*solid line*) and an inter-plume region (*dashed line*) for O VI 1037 Å and C II 1037 Å. From Banerjee *et al.* (2000).

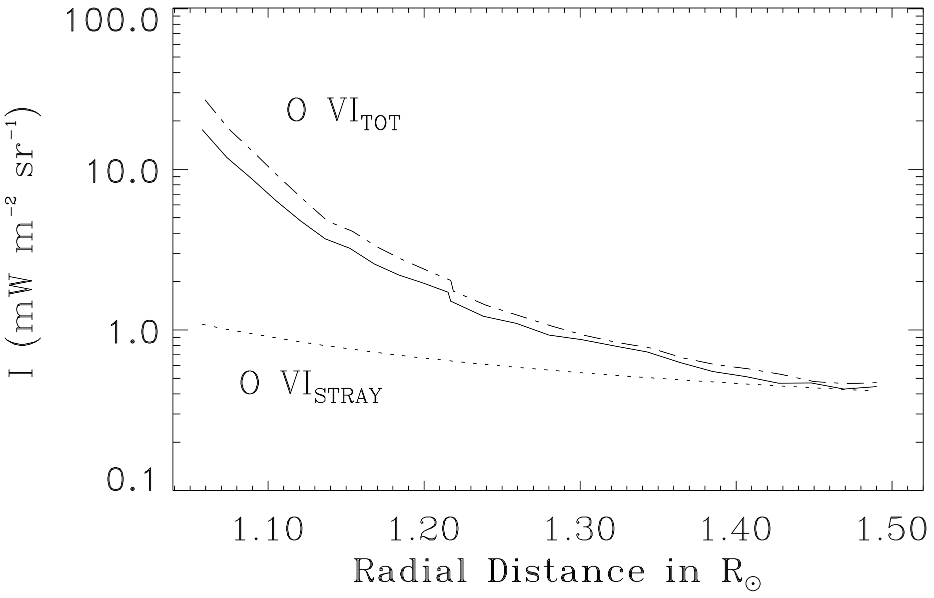

Figure 2.4: Variation of the O VI 1032 Å line intensity with height in the north polar coronal hole along a polar plume (*dot-dashed line*) and inter plume regions (*solid line*). The dotted line represents the stray light contribution to the O VI line intensity (adapted from Banerjee *et al.* 2000).

is entirely due to stray light (Lemaire *et al.* 1997).

Differences coming from the use of different detector and slit (in the case of the March 1997 observations) were taken into account in determining the width of the stray light profile. Assuming that the width of the O VI 1032 Å stray light profile does not vary with the height above the limb, its amplitude variation can be inferred from the stray light trend derived above. This allows the authors to obtain the stray light profile as a function of height and, finally, to remove it from the observed O VI profile. In Fig 2.4 (page 35) it is shown the variation of the O VI 1032 Å line intensity with height in the north polar coronal hole along a polar plume (*dot-dashed line*) and an inter-plume region (*solid line*). The dotted line represents the stray light contribution to the O VI line intensity. It clearly shows that, above 1.4 solar radii, the O VI intensity is entirely due to stray light.

Acknowledgements

L. Teriaca wish to thank Prof. J.G. Doyle at Armagh Observatory for revising and addressing his Ph.D. (Teriaca 2001), upon which this contribution is based. We thank Dr. Udo Schühle for very useful comments to the manuscript.

References

Banerjee D, Teriaca L., Doyle J.G., Lemaire P., 2000, *Polar Plumes and Interplume regions as observed by SUMER on SOHO*, Solar phys. 194, 43

Behring W.E., Cohen L., Doschek G.A., Feldman U., 1976, *The solar spectrum - Wavelengths and identifications from 160 to 770 angstroms*, ApJ 203, 521

Brynildsen N., Brekke P., Fredvik T., Haugan S.V.H., Kjeldseth-Moe O., Maltby P., Harrison R.A., Wilhelm K., 1998, *SOHO Observations of the Connection Between Line Profile Parameters in Active and Quiet Regions and the Net Redshift in EUV Emission Lines*, Solar Phys. 181, 23

Carlsson M., Judge P.G., Wilhelm K., 1997, *SUMER Observations Confirm the Dynamic Nature of the Quiet Solar Outer Atmosphere: The Internetwork Chromosphere*, ApJ 486, L63

Chae J., Yun H.S., Poland A.I., 1998a,*Temperature Dependence of Ultraviolet Line Average Doppler Shifts in the Quiet Sun*, ApJ S 114, 151

Chae J., Schühle U., Lemaire F., 1998b, *SUMER Measurements of Nonthermal Motions: Constraints on Coronal Heating Mechanisms*, ApJ 505, 957

Cohen L., Feldman U., Doschek G.A., 1978, *XUV spectra of the 1973 June 15 solar flare observed from Skylab. III - A list of spectral lines from 1000 to 1940 A*, ApJ S 37, 393

Curdt W., Feldman U., Laming J.M., Wilhelm K., Schühle U., Lemaire P., 1997a, *The solar disk spectrum between 660 and 1175 Angstroms (first order) obtained by SUMER on SOHO*, A&A S 126, 281

Curdt W., Kučera A., Rybák J., Schühle U., Wöhl H., 1997b, *Dynamical properties of the chromosphere and transition region in the supergranular network: what precision of the spectral line characteristics can be reached?*, Proceedings of the fifth SOHO Workshop, The corona and solar wind near minimum activity, ESA SP-404, 307

Curdt W., Brekke P., Feldman U., Wilhelm K., Dwivedi B.N., Schühle U., Lemaire P., 2001, *The SUMER spectral atlas of solar-disk features*, A&A 375, 591

Dammasch I.E., Wilhelm K., Curdt W., Hassler D.M., 1999, *The Ne* VIII *(lambda 770) resonance line: solar wavelengths determined by SUMER on SOHO*, A&A 346, 285

David C., Gabriel A.H., Bely-Dubau F., Fludra A., Lemaire P., Wilhelm K., 1998, *Measurement of the electron temperature gradient in a solar coronal hole*, A&A 336, L90

Dere K.P., Landi E., Mason H.E., Monsignori Fossi B.C., Young P.R., 1997, *CHIANTI - an atomic database for emission lines*, A&A S 125, 149

Feldman U., Behring W.E., Curdt W., Schühle U., Wilhelm K., Lemaire P., Moran T.M., 1997, *A Coronal Spectrum in the 500–1610 Angstrom Wavelength Range Recorded at a Height of 21,000 Kilometers above the West Solar Limb by the SUMER Instrument on Solar and Heliospheric Observatory*, ApJ S 113, 195

Gray D.F., 1992, *The observation and analysis of stellar photosphere*, Cambridge University Press, Cambridge

Grevesse N., Sauval A.J., 1998, *Standard Solar Composition*, Spa. Sci. Rev. 85, 161

Griffiths N.W., Aivieau S., Siegmund O.H.W., 1998, *In-flight performance of the*

SUMER microchannel plate detectors, Proc. SPIE 3445, 566

Hassler D.M., Rottman G.J., Orrall F.Q., 1991, *Systematic radial flows in the chromosphere, transition region, and corona of the quiet sun*, ApJ 372, 710

Hassler D.M., Wilhelm K., Lemaire P., Schühle U., 1997, *Observations of Polar Plumes with the SUMER Instrument on SOHO*, Solar Phys. 175, 375

Hollandt J., Schühle U., Paustian W., *et al.*, 1996, Appl. Opt. 35, 5125

Huber M.C.E., Dupree A.K., Goldberg L., Noyes R.W., Parkinson W.H., Reeves E.M., Withbroe G.L., 1973, *The Harvard Experiment on OSO-6: Instrumentation, Calibration, Operation, and Description of Observations*, ApJ 183, 291

Kelly R.L., 1982, Atomic and Ionic Spectrum Lines Below 2000 Angstroms, Oak Ridge National Laboratory, Tennessee (U.S.)

Kelly R.L., 1985, Spectroscopic Data for Iron, W.L. Wiese (ed.), National Bureau of Standards (U.S.)

Kelly R.L., 1987, J. Phys. Chem. Ref. Data 16, Suppl. No. 1

Kink I., Jupén C., Engström L., Feldman U., Laming J.M., Schühle U., 1997, *Laboratory Identification of Temperature Diagnostic SI VII and S IX Lines Present in the Solar Coronal Spectra Measured by SUMER/SOHO*, ApJ 487, 956

Landi E., Landini M., Dere K.P., Young P.R., Mason H.E., 1999, *CHIANTI - an atomic database for emission lines. III. Continuum radiation and extension of the ion database*, A&A S 135, 339

Landi E., Mason H.E., Lemaire P., Landini M., 2000, *SUMER observations of transition region fine structures*, A&A 357, 743

Lemaire P., 1991, Sensitivity changes in the CNRS ultraviolet spectrometer aboard OSO-8, ESA J. 15, 237

Lemaire P., Wilhelm K., Curdt W., Schühle U., Marsch E., Poland A.I., Jordan

S.D., Thomas R.J., Hassler D.M., Vial J.C., Kuhne M., Huber M.C.E., Siegmund O.H.W., Gabriel A., Timothy J.G., Grewing M., 1997, *First Results of the SUMER Telescope and Spectrometer on SOHO - II. Imagery and Data Management*, Solar Phys. 170, 105

Mariska J.T., 1992, 'The Solar Transition Region', Cambridge University Press, Cambridge

Mazzotta P., Mazzitelli G., Colafrancesco S., Vittorio N., 1998, *Ionization balance for optically thin plasmas: Rate coefficients for all atoms and ions of the elements H to Ni*, A&A S 133, 403

Moran T.G., 2002, Review of Scientific Instruments 73, iss. no. 11, p. 3982

Muglach K., Fleck B., 1999, *Waves in the quiet Sun's chromosphere*, Proceedings of 8^{th} Soho workshop, Plasma dynamics and diagnostics in the solar transition region and corona, ESA SP-446, 499

Noyes R.W., Raymond J.C., Doyle J.G., Kingston A.E., 1985, *The extreme ultraviolet spectrum of sunspot plumes. I - Observations*, ApJ 297, 805

Peter H., 1999a, *Analysis of Transition-Region Emission-Line Profiles from Full-Disk Scans of the Sun Using the SUMER Instrument on SOHO*, ApJ 516, 490

Peter H., 1999b, *The Chromosphere in Coronal Holes and the Quiet-Sun Network: an HE I (584) Full-Disk Scan by SUMER/SOHO*, ApJ 522, L77

Peter H., Judge P.G., 1999, *On the Doppler Shifts of Solar Ultraviolet Emission Lines*, ApJ 522, 1148

Reeves E.M., Timothy J.G., Withbroe G.L., Huber M.C.E., 1977, *Photometric calibration of the EUV spectroheliometer on ATM*, Appl. Opt. 16, 849

Rybák J., Curdt W., Kučera A., Schühle U., Wöhl H., 1999a, *SoHO/SUMER Chromospheric and Transition Region Dynamics – Reasons and Consequences of* *the Long-period Instrumental Periodicities of SUMER/SOHO*, Proceedings of the Ninth European Meeting on Solar Physics: Magnetic Fields and Solar Processes, ESA SP-448, 361

Rybák J., Curdt W., Kučera A., Schühle U., Wöhl H., 1999b, *SoHO/SUMER Chromospheric and Transition Region Dynamics – Reasons and Consequences of the Short period Instrumental Periodicities of SUMER/SOHO*, Proceedings of the 8^{th} Soho Workshop: Plasma dynamics and diagnostics in the solar transition region and corona, ESA SP-446, 579

Samain D., 1991, *Is the ultraviolet spectrum of the quiet sun redshifted?*, A&A 244, 217

Sandlin, G.D., Bartoe J.-D.F., Brueckner G.E., Tousey R., Vanhoosier M.E., 1986, *The high-resolution solar spectrum, 1175-1710 A*, ApJ S 61, 801

Schühle U., Brekke P., Curdt W., Hollandt J., Lemaire P., Wilhelm K., 1998, *Radiometric Calibration Tracking of the Vacuum-Ultraviolet Spectrometer SUMER During the First Year of the SOHO Mission*, Appl. Opt. 37, 2646

Schühle U., Curdt W., Hollandt J., Feldman U., Lemaire P., Wilhelm K., 2000, *Radiometric Calibration of the Vacuum-Ultraviolet Spectrograph SUMER on SOHO with the B Detector*, Appl. Opt. 39, 418

Schühle U., Curdt W., Hollandt J., Feldman U., Lemaire P., Wilhelm K., 2000, *Radiometric Calibration of the Vacuum-Ultraviolet Spectrograph SUMER on SOHO with the B Detector*, Appl. Opt. 39, 418

Schühle U., 2003, *Cleanliness and Calibration Stability of UV Instruments on SOHO*, Proc. SPIE 4853, 88

Siegmund O.H., Stock J.M., Marsh D.R., Gummin M.A., Raffanti R., Hull J., Gaines G.A., Welsh B.Y., Donakowski B., Jelinsky P.N., Sasseen T., Tom J.L., Higgins B., Magoncelli T., Hamilton J.W., Battel S.J., Poland A.I., Jhabvala

M.D., Sizemore K., Shannon J., 1994, *Delay-line detectors for the UVCS and SUMER instruments on the SOHO Satellite*, Proc SPIE 2280, 89

Steward T.B., Arnold G.S., Hall F., Marten H.D., 1989, *Photolysis of spacecraft contaminants*, Report SD-TR-89-45, The Aerospace Corporation, El Segundo, California

Teriaca L., 2001, *Structure and dynamics of the solar outer atmosphere as inferred from EUV observations*, Ph.D. Thesis, The Queen's University of Belfast/Armagh Observatory

Teriaca L., Banerjee D., Doyle J.G., 1999, *SUMER observations of Doppler shift in the quiet Sun and in an active region*, A&A 349, 636

Vernazza J.E., Reeves E.M., 1978, *Extreme ultraviolet composite spectra of representative solar features*, ApJ S 37, 485

Waljeski K., Moses D., Dere K.P., Saba J.L.R., Strong K.T., Webb D.F., Zarro D.M., 1994, *The composition of a coronal active region*, ApJ 429, 909

Warren H.P., Mariska J.T., Wilhelm K., Lemaire P., 1997, *Doppler Shifts and Nonthermal Broadening in the Quiet Solar Transition Region: O VI*, ApJ 484, L91

Wilhelm K., Curdt W., Marsch E., Schühle U., Lemaire P., Gabriel A., Vial J.-C., Grewing M., Huber M.C.E., Jordan S.D., Poland A.I., Thomas R.J., Kühne M., Timothy J.G., Hassler D.M., Siegmund O.H.W., 1995, *SUMER - Solar Ultraviolet Measurements of Emitted Radiation*, Solar Phys. 162, 189

Wilhelm K., Lemaire P., Curdt W., Schühle U., Marsch E., Poland A.I., Jordan S.D., Thomas R.J., Hassler D.M., Huber M.C.E., Vial J.-C., Kühne M., Siegmund O.H.W., Gabriel A., Timothy J.G., Grewing M., Feldman U., Hollandt J., Brekke P., 1997, *First Results of the SUMER Telescope and Spectrometer on SOHO - I. Spectra and Spectroradiometry*, Solar Phys. 170, 75

Wilhelm K., Woods T.N., Schühle U., Curdt W., Lemaire P., Rottman G.J., 1999, *The Solar Ultraviolet Spectrum from 1200 Åto 1560 Å: A Radiometric Comparison between SUMER/SOHO and SOLSTICE/UARS*, A&A 352, 321

Wilhelm K., Schühle U., Curdt W., Dammasch I.E., Hollandt J., Lemaire P., Huber M.C.E., 2000, *Solar spectroradiometry with SUMER on SOHO*, Metrologia, 37(5), 393

Woods T.N., Rottman G.J., Bailey S.M., Solomon S.C., Worden J.R., 1998, *Solar Extreme Ultraviolet Irradiance Measurements During Solar Cycle 22*, Solar Phys. 177, 133